RECONSTRUCTION FROM PROJECTIONS BASED ON DETECTION AND ESTIMATION OF OBJECTS
PART I: Performance Analysis

David J. Rossi
Schlumberger-Doll Research
P.O. Box 307
Ridgefield, CT 06877

Alan S. Willsky
Room 35-233, M.I.T.
77 Massachusetts Avenue
Cambridge, MA 02139

ABSTRACT

The problem of reconstructing a multi-dimensional field from noisy, limited projection measurements is approached using an object-based stochastic field model. Objects within a cross-section are characterized by a finite-dimensional set of parameters, which are estimated *directly* from limited, noisy projection measurements using maximum likelihood estimation. In Part I, the computational structure and performance of the ML estimation procedure are investigated for the problem of locating a single object in a deterministic background; simulations are also presented. In Part II, the issue of robustness to modeling errors is addressed.

I. INTRODUCTION

The problem of reconstructing an n-dimensional function from its (n-1)-dimensional projections arises, typically in the context of cross-sectional imaging, in a diversity of disciplines. In the two-dimensional (2D) problem, let $f(x)$ represent the value of the cross-sectional function (for example x-ray attenuation coefficient) at a point specified by the vector $x = (x_1 \ x_2)'$. The *projection* of $f(x)$ at any angle θ is a 1D function denoted as $g(t,\theta)$ shown in Figure 1. For a given value of projection angle θ, the projection evaluated at the point t is the integral

$$g(t,\theta) = \int_{-\infty}^{\infty}\int_{-\infty}^{\infty} f(x)\,\delta(t-x'\theta)\,dx_1\,dx_2 = \int_{x'\theta=t} f(x)\,ds \triangleq [Rf](t,\theta) \qquad (1)$$

along the line

$$l(t,\theta) = \{x : x_1\cos\theta + x_2\sin\theta = t\} = \{x : x'\theta = t\} \qquad (2)$$

$$\theta \triangleq (\cos\theta \quad \sin\theta)'$$

$$(t,\theta) \in Y \triangleq \{(t,\theta) : -\infty < t < \infty \ , \ 0 \leq \theta < \pi\}$$

as shown in Figure 2. In (1), $\delta(t)$ is the Dirac delta function. Equation (1) corresponds to the *Radon transformation*, which maps the 2D function $f: R^2 \rightarrow R$ into the function on a half-cylinder $g: Y \rightarrow R$; $g(t,\theta)$ is called the Radon transform of $f(x)$ [1-3], and is also denoted by $[Rf](t,\theta)$. The reconstruction problem, determining the function f from its projections g, is an inverse problem, since the measurements are specified by the integral equation in (1) which must be inverted to recover an estimate of the original function.

Reconstruction from projections has been employed successfully in radio astronomy, electron microscopy, medical CAT scanning and other applications. Recently, it has been suggested that these techniques be similarly applied to a number of technologically demanding and novel applications, for example real-time monitoring of high production rate manufacturing processes, mesoscale oceanographic thermal mapping, quality control nondestructive evaluation, and "stop action" imaging of very rapidly changing media [4,5]. Virtually all of these applications, as well as many current applications, are characterized by a limited availability of measurement data, due to:

- economic constraints that limit the total number of measurement transducers -- e.g. oceanographic transducers are sophisticated, low power units that are costly to build, place and maintain [5].

- time constraints that limit measurement quality -- e.g. limited measurement time interval in "stop action" imaging of very rapid events, or in nondestructive testing of high production rate processes such as steel manufacturing [4].

- safety and operating constraints that limit the measurement quality -- e.g. high temperature and/or caustic operating environments in certain process monitoring applications may limit sensor accuracy and SNR performance; in medical tomography, patient safety constrains the overall x-ray or injected radionuclide dose [12].

- geometrical or physical constraints that limit the view angle -- e.g. in ultrasonic imaging of the heart, where bony structures limit the view angle, or in nondestructive testing of large objects.

- inaccuracy of the measurement model -- the simple line integral measurement model in (1) is an idealization that does not incorporate, for example, the effects of refraction, diffraction, scattering and polychromaticity.

It is well known, however, that when the projection measurements are limited in number or view angle, or have high noise levels, the inverse problem is ill-posed and/or has a numerically sensitive or noisy solution [1,2,11,12] -- that is, it is not possible to reliably produce accurate, artifact-free and high-resolution imagery of the cross-section.

In a number of applications, particularly applications where the measurement data are limited, the *ultimate* goal of processing the projection measurements is typically far more modest than obtaining high-resolution cross-sectional imagery. Rather, reconstructed imagery is an intermediate result of the overall analysis, and is itself processed (either visually or by automated or semi-automated techniques) to extract very particular information about the cross-section.

In many cases, this particular information is related to objects, regions or boundaries within the cross-section. For example, in medical CAT scanning, the detection, localization and characterization of organs and tumors is a routine step in diagnostic interpretation [6,7]; the localization and identification of boundaries of high-contrast objects such as bone and metallic surgical clips by direct processing of projection data has also been studied [8]. Another application where object-related information is desired is oceanography; large, high-contrast thermal regions are present in many oceans (e.g. cold-core rings [5] and the Gulf stream), and oceanographic acoustic tomography has been investigated as a means of detecting and tracking these regions [5,9]. In the area of non-destructive evaluation, tomographic techniques have also been studied for detecting and characterizing interior cracks and flaws in materials [10].

The focus of this paper is on processing projection measurements when (1) the overall goal is to extract object-related information about the cross-section, and (2) limitations on the total number, SNR, or overall view angle of the projection measurements preclude the formation of high-resolution, artifact-free reconstructed imagery. In particular, an alternative to full image reconstruction is proposed and investigated that involves processing limited, noisy projection measurements *directly*, in order to detect, locate and characterize one or more objects within the cross-section. Specifically, a stochastic, object-based field model is presented, in which objects are represented by a finite number of parameters, characterizing, say, the object location, size, boundary shape, contrast, and/or detailed internal density variations. These parameters are estimated, for the case of limited projection measurements corrupted by additive white Gaussian noise, by maximum likelihood (ML) parameter estimation [13].

While it is possible to present procedures which may be applied to cross-sections containing arbitrarily complex arrangements of objects and boundaries, the focus is rather on a simpler problem, in order to lay bare the problem essentials. The specific problem considered is estimation of the *location* of a single, randomly-located object situated within a known background field; problems of this type, involving detection of objects in an otherwise completely known field have been of interest for some time in radiology [6]. Concentrating on this specific localization problem allows (1) the development of insight into the computational structure of the parameter estimation (the computation is shown to resemble one solution to the image reconstruction problem, namely the convolution back-projection (CBP) inversion formula [1]), (2) the demonstration of quantitative tools that can be utilized in critically evaluating estimator performance and robustness in a systematic manner, and (3) the establishment of a framework within which more sophisticated algorithms may be developed which take into account, for example, detailed a priori information about

object boundary shapes, or the presence of multiple objects. One particular result obtained which demonstrates the potential utility of this approach is identification of the minimum size of an object that can be located from given noisy projection measurements.

In developing the relatively simple localization problem, a number of simplifications are necessarily made. The robustness analysis in Part II assesses the robustness of ML object localization when applied to less idealized versions of the problem, taking into account, for example, that the real object may have a shape and density that differ from the simple assumed shape and density, or that additional, unmodeled objects may be present within the cross-section. This robustness analysis, by providing insight into the sensitivity of the performance to different types of modeling errors, in turn provides intuition about potentially useful extensions or improvements in the development of more sophisticated algorithms.

In the next section, (i) a simple stochastic, object-based model for the cross-section is introduced, as are models for discrete and continuous measurements, and (ii) the ML object localization problem is formulated. In Section III, the error covariance of the ML location estimate is examined; both local and global errors are treated. In Sections IV and V, an example and simulations are presented which illustrate the localization of an object having a simple geometric shape.

II. PRELIMINARY ANALYSIS

Cross-sectional Model

Suppose the cross-section under investigation is represented as a known *background* function $f_b(x)$, superimposed upon which is a single "object" -- an object will be modeled as a 2D function that is an additive component of the overall cross-sectional density. The overall cross-sectional density, then, is of the form

$$f(x) = f_b(x) + d \cdot f_0(x-c) \tag{3}$$

where d represents the brightness or contrast of the object, $f_0(x)$ corresponds to a unit-contrast object situated at the origin, and $c = (c_1 \ c_2)'$ denotes the object location in the plane.[1] Note that because the function $f(x)$ depends nonlinearly (by a shift in x) on the object location, the problem of estimating c from measurements of $f(x)$ (or its integrals) is a nonlinear estimation problem. This is in contrast to direct image reconstruction, in which a linear estimation problem of considerably higher dimensionality is solved.

As an example of the representation in (3), consider the problem of locating a connected region K (e.g. a disk) having constant density d relative to the background. In this case, the object is a discontinuous function that equals zero everywhere except at points within the set K, where it takes on the value d. Alternatively, a circularly-symmetric object of radius R and density d may be described by using a Gaussian object $f_0(x) = \exp(-\|x\|^2 / R^2)$, where $\|x\|$ is the distance of the point x from the origin. See [14] for a discussion of these and other continuous and discontinuous object

---

1. More generally, the object may depend on a finite number of parameters characterizing, say, its size, shape and/or detailed boundary, and these parameters may be estimated [14].

models. In Sections IV and V, results are illustrated using as an example a discontinuous object that has a constant density on a disk.

Measurement Model

The cross-sectional density function f(x) can be observed only via limited, noisy projections. Two types of measurements are considered here, specifically, projection measurements taken over a *continuous* interval of view angle values θ and projection measurements taken at only a finite number of *discrete* projection angles. In both cases, the measurement at angle θ will be modeled as the convolution of the continuous 1D projection g(t,θ;c) (which depends on the object location c) with a 1D measurement aperture h(t), and corrupted by additive zero-mean white Gaussian noise,[2]

$$y(t,\theta) = g(t,\theta;c) * h(t) + w(t,\theta)$$

$$\triangleq s(t,\theta;c) + w(t,\theta) \qquad (t,\theta) \in S \subset Y \qquad (4)$$

Various aperture functions may be considered, for example a rectangular pulse aperture corresponding to strip integration, an impulsive aperture corresponding to line integration, or the sinc aperture

$$h(t) = \frac{\sin 2\pi Wt}{2\pi Wt} \qquad (5)$$

corresponding to projections having a spatial bandwidth of W cycles per unit distance in the t direction. The use of a nonimpulsive measurement aperture h(t) facilitates the modeling of finite bandwidth projection measurements.

Case 1: Continuous-view Measurements

In the continuous-view case, measurements are taken over a total viewing angle of 2Δ centered at $\frac{\pi}{2}$, i.e., views are taken up to an angle Δ on either side of the x_1 axis (here, $0 < \Delta \leq \frac{\pi}{2}$). The measurement set S is a subset of the half-cylinder Y, and is given by

$$S = S_\Delta \triangleq \{(t,\theta) : -\infty < t < \infty , \frac{\pi}{2} - \Delta \leq \theta < \frac{\pi}{2} + \Delta\} \qquad (6)$$

In the continuous-view case, the additive noise w(t,θ) is a 2D zero-mean Gaussian random field on S_Δ with covariance

$$E\{w(t,\theta)w(\tau,\phi)\} = \frac{N_0}{2} \delta(t-\tau,\theta-\phi) \qquad (7)$$

where $\delta(t,\theta)$ is a 2D impulse. The standard tomographic reconstruction problem, where (noise-free) measurements are assumed to be available at all possible projection angles, is the special case of the continuous-view measurement case where $\Delta = \frac{\pi}{2}$. This will be referred to as the *full-view*

---

2. y(t,θ) could also be considered as a counting process with a rate that depends on g(t,θ;c). Such a model is appropriate, for example, in very low-dose X-ray problems.

measurement case, and the case $\Delta < \frac{\pi}{2}$ will be referred to as the *limited-view* measurement case.

Case 2: Discrete-view Measurements

In the discrete-view case, projections are measured at N angles that are uniformly spaced on the interval $[0,\pi)$. The measurement subset is

$$S = S_N \triangleq \{(t,\theta) : -\infty < t < \infty \ , \ \theta = \theta_j = \frac{j\pi}{N} \ \ j = 0,1,\ldots,N-1\} \tag{8}$$

For each view angle θ_j, the noise process $w(t,\theta_j)$ is a 1D zero-mean Gaussian process with covariance

$$E\{w(t,\theta_j)\,w(\tau,\theta_j)\} = \frac{N_0}{2}\,\delta(t-\tau) \tag{9}$$

and the noise at different view angles θ_i and θ_j , $i \neq j$, is uncorrelated.

For the cross-sectional density function shown in (3), the Radon transform (1) is

$$g(t,\theta) = \int\limits_{x'\theta=t} f_b(x)\,ds + d\int\limits_{x'\theta=t} f_0(x-c)\,ds \tag{10}$$

Since the background function is known, the first term in (10) is known and may be subtracted from the Radon transform (this is assumed to be done for the remainder of this analysis) to leave the part due solely to the object, namely

$$g(t,\theta;c) = d\int\limits_{x'\theta=t} f_0(x-c)\,ds \tag{11}$$

Let $g_0(t,\theta)$ denote the Radon transform when the object is located at the origin,

$$g_0(t,\theta) \triangleq g(t,\theta;0) = d\int\limits_{x'\theta=t} f_0(x)\,ds \tag{12}$$

For an arbitrary object location $c \in C \subset R^2$, the Radon transform is, from (11) and (12),

$$g(t,\theta;c) = d\int\limits_{x'\theta=t-c'\theta} f_0(x)\,ds = g_0(t-c'\theta,\theta) \tag{13}$$

Equation (13) indicates the nonlinear dependence of the Radon transform $g(t,\theta;c)$ on the object location. Specifically, when an object is translated from the origin to the point c, its Radon transform experiences a shift in the t variable, where the magnitude of this shift, $c'\theta = c_1\cos\theta + c_2\sin\theta$, depends sinusoidally on θ.

Example 1

Consider a constant-density object on a disk of radius R centered at the point c in the plane (see Figure 3a),

$$d\cdot f_0(x-c) = \begin{cases} d & \text{if } \|x-c\| \leq R \\ 0 & \text{otherwise} \end{cases} \tag{14}$$

For any value of θ, the projection $g(t,\theta;c)$ is a half-ellipse centered at $t=c'\theta$,

$$g(t,\theta;c) = \begin{cases} 2d\sqrt{R^2 - (t - c'\theta)^2} & \text{if } |t - c'\theta| \leq R \\ 0 & \text{otherwise} \end{cases} \tag{15}$$

This Radon transform, viewed as a function $g: Y \rightarrow R$ is the θ-dependent function shown in Figure 3b. Note that while in this example the object $f_0(x)$ is circularly-symmetric, an object is generally not circularly-symmetric, and consequently its Radon transform $g_0(t,\theta)$ is θ-dependent and nonsymmetric.

Maximum Likelihood Location Estimation

Given a set of continuous- or discrete-view measurements $y(t,\theta)$, it is desired to estimate the object location c by maximum likelihood (ML) estimation. The ML location estimate is obtained by first using the projection measurements to compute a log likelihood function $L(c)$, and then finding the 2D parameter $c \in C \subset R^2$ at which the maximum value occurs.

In the continuous-view case with a total viewing angle of 2Δ, the log likelihood function is given by [13]

$$L_\Delta(c) = \frac{2}{N_0} \int_{\frac{\pi}{2}-\Delta}^{\frac{\pi}{2}+\Delta} \int_{-\infty}^{\infty} y(t,\theta)\, s(t,\theta;c)\, dt\, d\theta - \frac{1}{N_0} \int_{\frac{\pi}{2}-\Delta}^{\frac{\pi}{2}+\Delta} \int_{-\infty}^{\infty} s^2(t,\theta;c)\, dt\, d\theta \tag{16a}$$

and in the discrete-view case with a total of N views, it is given by

$$L_N(c) = \frac{2}{N_0} \sum_{j=0}^{N-1} \int_{-\infty}^{\infty} y(t,\theta_j)\, s(t,\theta_j;c)\, dt - \frac{1}{N_0} \sum_{j=0}^{N-1} \int_{-\infty}^{\infty} s^2(t,\theta_j;c)\, dt \tag{16b}$$

In each case, the log likelihood function is the difference between two terms, the first of which is obtained by a matched filtering operation [13] on the measurements using a filtering template $s(t,\theta;c)$. The second term compensates for the filtering template energy. From (4), (13), and a change of variable

$$\int_{-\infty}^{\infty} s^2(t,\theta;c)\, dt = \int_{-\infty}^{\infty} s^2(t - c'\theta,\theta;0)\, dt = \int_{-\infty}^{\infty} s^2(\tau,\theta;0)\, d\tau \tag{17}$$

The final integral in (17) is c-independent, so the matched filter template energy terms in (16) are constant and may be dropped, as can the first term scaling constant, leaving

$$L_\Delta(c) = \int_{\frac{\pi}{2}-\Delta}^{\frac{\pi}{2}+\Delta} \int_{-\infty}^{\infty} y(t,\theta)\, s_0(t - c'\theta,\theta)\, dt\, d\theta \tag{18a}$$

and

$$L_N(c) = \sum_{j=0}^{N-1} \int_{-\infty}^{\infty} y(t,\theta_j)\, s_0(t - c'\theta_j,\theta_j)\, dt \tag{18b}$$

where $s_0(t,\theta) \triangleq s(t,\theta;0) = g_0(t,\theta) * h(t)$.

In summary, the ML estimate for the object location is determined by computing the log likelihood function in (18), and determining the value of the two-dimensional parameter $c \in C$ at which the peak of the log likelihood function occurs,

$$\hat{c}_{ML} = \begin{cases} \underset{c \in C}{\text{argmax}} \, L_\Delta(c) & \text{in the continuous-view case} \\ \underset{c \in C}{\text{argmax}} \, L_N(c) & \text{in the discrete-view case} \end{cases} \tag{19}$$

Remarks

The convolution back-projection (CBP) inversion formula [1-3] is one solution to the integral equation in (1); it assumes the availability of noise-free full-view measurements and is given by

$$\hat{f}(x) = \int_0^\pi \int_{-\infty}^\infty g(t,\theta) \, v(t - x'\theta,\theta) \, dt \, d\theta = \int_0^\pi q(x'\theta,\theta) \, d\theta \triangleq [Bq](x) \tag{20}$$

This mapping of $g \rightarrow \hat{f}$ is refered to as a convolution back-projection operation. For perfect reconstruction from full-view noise-free projections, the convolving kernel $v(t,\theta)$ is θ-independent, and its Fourier transform with resect to t satisfies $V(\omega) = |\omega|$ [1,2]. The so-called *back-projection* operator (the integral with respect to θ) maps the function $q: Y \rightarrow R$ into the 2D function $\hat{f}: R^2 \rightarrow R$, the latter function $\hat{f}(x)$ is called the back-projection of q and is denoted by $[Bq](x)$ [3].

Consider the case of full-view measurements $(\Delta = \frac{\pi}{2})$, and notice the similarity between the log likelihood function in (18a) and the convolution back-projection inversion formula in (20). In (20), the noise-free projection measurements $g(t,\theta)$ are used to determine a 2D reconstruction $\hat{f}(x)$ by convolution back-projection with a θ-independent convolving kernel $v(t)$. In (18a) with $\Delta = \frac{\pi}{2}$, the noisy projection measurements $y(t,\theta)$ are used to determine a 2D log likelihood function by convolution back-projection with a generally θ-dependent and nonsymmetric convolving kernel $s_0(t,\theta)$

Note that although (18a) may be interpreted as a CBP, the resulting log likelihood function is *not* interpreted as a reconstructed image because the convolving kernel is not chosen with direct image reconstruction in mind. Rather, the convolving kernel $s_0(t,\theta)$ is specified in the solution to the problem of ML estimation of the object location from noisy projection data.

In the limited-view case $(\Delta < \frac{\pi}{2})$, and in the discrete-view case, the log likelihood function in (18) still has the same general form as the CBP operation in (20), except that the integral with respect to θ for $\theta \in [0,\pi)$ (i.e. the back-projection operation) is replaced by either an integral with respect to θ for $\theta \in [\frac{\pi}{2} - \Delta, \frac{\pi}{2} + \Delta)$ or by an N-point sum over θ_j. These expressions resemble those associated with *approximate convolution back-projection reconstruction algorithms* [3]. These are practical implementations of the

reconstruction formula in (20) that are used to compute approximate reconstructed images when measurements are available only on some subset of the full measurement set Y. The distinction between reconstructing an image using (20) and evaluating a log likelihood function using (18) still applies.

In terms of computational complexity, direct image reconstruction and log likelihood function evaluation both involve the determination of a 2D function whose value at any point is given by an integral or sum of weighted projection data. Consequently, both procedures require the same amount of computation for a given set of measurements. If the overall goal of the signal processing is to locate an object within a cross-section, however, the task is completed when the log likelihood function peak is found. In contrast, when a reconstructed image is formed, further image processing (e.g. 2D pre-whitening and matched filtering) is required if the location of the object is to be determined.

Thus far a parametric object-based field model has been put forth and the problem of ML estimation of object location using noisy projection measurements has been formulated. Several performance-related questions arise: (1) if the actual cross-section satisfies the modeling assumptions exactly, how well can the object parameters be estimated from noisy projection data? and (2) modeling errors inevitably exist; when the model is an inaccurate representation of the actual cross-section, how well can the object parameters be estimated?

The latter question is addressed in the robustness analysis of Part II. In the remainder of Part I, it is assumed that no modeling inaccuracies exist, and the former issue is investigated. The overall object location estimate error covariance, characterized by both local and global contributions, is analyzed in Section III. In this development, algorithmic or implementation issues such as efficient procedures for locating the log likelihood function peak are not discussed; instead, issues of how well one can do assuming that the ML estimation procedures can be carried out exactly will serve as the focus. In Sections IV and V, the error covariance is evaluated and computer simulations are presented for the constant-density disk object of Example 1.

III. PERFORMANCE ANALYSIS

The maximum likelihood estimate for the location of an object in the cross-section is obtained from projection measurements by first performing a CBP operation to obtain the 2D log likelihood function shown in (18), and then finding the point $c \in C$ at which the maximum occurs. As suggested by the similarity between (18a) and (18b), the calculation of the log likelihood function for the continuous- and discrete-view measurement cases are very similar, and the general concepts involved in the continuous-view performance analysis carry over directly to the discrete-view case, although the details of the analysis differ [14]. Due to the similarity in the calculations, only the continuous-view computations will be detailed here.

Because the measurements $y(t,\theta)$ are noisy, the location log likelihood function is a 2D random field. The point $\hat{c}_{ML} \in C$ that maximizes this random field is a 2D random variable; in this performance analysis the second moment of this 2D random variable is characterized. First, to see how the log likelihood function depends on the

measurement noise, let c_a denote the actual object location within the cross-section, and substitute (4) into (18a)

$$\bar{L}_\Delta(c,c_a) = \int_{\frac{\tau}{2}-\Delta}^{\frac{\tau}{2}+\Delta} \int_{-\infty}^{\infty} s(t,\theta;c_a)\, s(t,\theta;c)\, dt\, d\theta + \int_{\frac{\tau}{2}-\Delta}^{\frac{\tau}{2}+\Delta} \int_{-\infty}^{\infty} w(t,\theta)\, s(t,\theta;c)\, dt\, d\theta$$

$$\overset{\Delta}{=} \bar{a}_\Delta(c,c_a) + n_\Delta(c) \tag{21}$$

The log likelihood function is the sum of two terms, $\bar{a}_\Delta(c,c_a)$, the expected value of the log likelihood function, which is a 2D deterministic function known as the *generalized ambiguity function* [17], and $n_\Delta(c)$, a 2D zero-mean correlated random field with covariance

$$E\{n_\Delta(c)n_\Delta(\tilde{c})\} = \frac{N_0}{2} \bar{a}_\Delta(c,\tilde{c}) \tag{22}$$

The ambiguity function, since it enters both the deterministic and random components of the log likelihood function, plays a key role in the analysis of estimation performance in the problem at hand, as it does in radar and sonar applications in the analysis of estimation accuracy, ambiguity, and resolution [17].

Because $s(t,\theta;c)$ depends on c only by a shift in the t variable, the ambiguity function may be shown by a change of variable to depend on its two arguments only through their difference. That is, the ambiguity function at any given point c depends only on the position of that point relative to the actual object location c_a. Consequently, the noise $n_\Delta(c)$ is stationary; for simplicity, the following notation for the ambiguity and log likelihood functions will be used

$$a_\Delta(\epsilon) \overset{\Delta}{=} \bar{a}_\Delta(c,c_a)$$

$$L_\Delta(\epsilon) \overset{\Delta}{=} \bar{L}_\Delta(c,c_a) \qquad\qquad \epsilon \overset{\Delta}{=} c - c_a \tag{23}$$

Estimation Error Covariance

At this point, the statistical accuracy of the location estimate $\hat{c}_{ML}$ will be investigated by considering Λ_e, the 2×2 error covariance matrix for the location estimate,

$$\Lambda_e = E\{e\,e'\} \qquad\qquad e \overset{\Delta}{=} \hat{c}_{ML} - c_a \tag{24}$$

One error analysis technique useful in nonlinear ML estimation problems is to write the error covariance as a linear combination of conditional error covariances, where each term is conditioned on the event that the estimate falls into a certain subset of the overall parameter space [13]. This approach is attractive because in many cases approximate conditional error covariances may be determined quite easily if the overall parameter space is partitioned judiciously.

To apply this technique, the set of possible parameter values C is partitioned into M nonoverlapping regions C_0, C_1, . . . , C_{M-1} (for example, rectangular subsets of the plane). Letting E_j denote the event that the peak of the log likelihood function

lies in region C_j, the error covariance may be expressed as

$$\Lambda_e = \sum_{j=0}^{M-1} \Lambda_j p_j \qquad\qquad p_j \triangleq \text{Prob}\{E_j\} \qquad (25)$$

where Λ_j denotes the estimate error covariance conditioned on E_j.

Two approximations are made at this time in order to simplify the analysis and provide an approximate expression for the error covariance Λ_e. As will be evident, the validity of these assumptions depends upon the choice of the C_j. In Section IV, a detailed example is provided which includes a discussion of how one can deduce the appropriate size for the C_j from knowledge of the ambiguity function.

1. Let $\{\gamma_j : \gamma_j \in C_j , j=0,1,...,M-1\}$ be a set of M points (with respect to a coordinate system centered at c_a), and for simplicity, assume that $\gamma_0 = c_a \in C_0$. Let $L_j \triangleq L_\Delta(\gamma_j)$, that is L_j is a random variable defined to be the log likelihood function in (23) evaluated at the point γ_j. Since the additive measurement noise $w(t,\theta)$ in (4) is Gaussian, the random vector $\underline{L} = (L_0 \ L_1 \ \cdots \ L_{M-1})'$ is Gaussian, with density $p(\underline{L})$ and moments

$$E\{L_j\} = a_\Delta(\gamma_j)$$

$$E\left\{ (L_i - E\{L_i\})(L_j - E\{L_j\}) \right\} = \frac{N_o}{2} a_\Delta(\gamma_i - \gamma_j) \qquad (26)$$

The first simplification which is made is to approximate the log likelihood function $L_\Delta(\epsilon)$ as being constant on each of the M regions, taking on the value L_j at *all* points in the region C_j, $j=0,1,...,M-1$. For this approximation to be good, the regions C_j should be sufficiently small in size so that random variables $L_\Delta(\gamma')$ and $L_\Delta(\gamma'')$ are highly correlated for any two points γ' and γ'' in C_j; this insures that the value L_j at a representative point γ_j is indicative of the log likelihood function value over the entire region C_j. When $L_\Delta(\epsilon)$ is thus approximated as being piecewise-constant, the computation of the probabilities p_j is simplified,

$$p_j = \text{Prob}\{L_j > L_i , \forall i \neq j\}$$

$$= \int_{-\infty}^{\infty} \left[\int_{-\infty}^{L_j} \cdots \int_{-\infty}^{L_j} p(\underline{L}) \, dL_0 \cdots dL_{M-1} \right] dL_j \qquad (27)$$

In practice, the probabilities p_j are computationally intensive to determine when the log likelihood function values L_j are correlated, although some work on bounds is available [18]. In the case of uncorrelated L_j, bounds such as the union bound [13] are more easily obtained (approximately uncorrelated L_j arise when the regions C_j are large in size).

2. The exact expression for the conditional error covariance Λ_j in (25) is given by

$$\Lambda_j = \int\int_{C_j} (\hat{c}-\gamma_0)(\hat{c}-\gamma_0)' \, p(\hat{c}|E_j)d\hat{c}_1 d\hat{c}_2$$

$$= \int\int_{C_j} [(\hat{c}-\gamma_j)+(\gamma_j-\gamma_0)][(\hat{c}-\gamma_j)+(\gamma_j-\gamma_0)]' p(\hat{c}|E_j)d\hat{c}_1 d\hat{c}_2 \qquad (28)$$

If γ_j is a representative point in C_j (e.g. the centroid), then conditioned on the event E_j, $j \neq 0$ (i.e. the event that the log likelihood function peak $\hat{c}$ lies in an incorrect region C_j), the magnitude of $\gamma_j - \gamma_0$ (between regions) is much larger than the magnitude of $\hat{c} - \gamma_j$ (within a region), and the conditional error covariance may be approximately written as

$$\Lambda_j \approx (\gamma_j - \gamma_0)(\gamma_j - \gamma_0)' \qquad j \neq 0 \qquad (29)$$

Using the approximation in (29), the error covariance in (25) may be written as

$$\Lambda_e = \begin{bmatrix} \sigma_{11}^2 & \sigma_{12}^2 \\ \sigma_{21}^2 & \sigma_{22}^2 \end{bmatrix} = \Lambda_0 P_0 + \sum_{j=1}^{M-1} (\gamma_j - \gamma_0)(\gamma_j - \gamma_0)' P_j \qquad (30)$$

In (30), Λ_0 is the error covariance conditioned on the event that the peak of the log likelihood function lies in C_0, the region containing the true location point. If the region C_0 is small enough so that all of its points are close to the true object location c_a, the Cramer-Rao bound [13] provides an accurate estimate of the covariance matrix Λ_0, and in particular, of its diagonal components. Specifically,

$$[\Lambda_0]_{ii} \geq [J^{-1}]_{ii} \qquad i \in \{1,2\} \qquad (31)$$

where J is the 2×2 Fisher's information matrix

$$[J]_{ik} = -E\left\{ \frac{\partial^2 L_\Delta(\epsilon)}{\partial \epsilon_i \partial \epsilon_k} \right\} \qquad i,k \in \{1,2\} \qquad (32)$$

and $L_\Delta(\epsilon)$ is the log likelihood function in (23). By taking derivatives of (21), (32) may be written in terms of the ambiguity function as

$$[J]_{ik} = -\frac{2}{N_o}\left[\frac{\partial^2 a(\epsilon)}{\partial \epsilon_i \partial \epsilon_k} \right]_{\epsilon=0} \Delta - \frac{2}{N_o}\beta_{ik} \qquad i,k \in \{1,2\} \qquad (33)$$

When the object location estimate $\hat{c}_{ML}$ lies in the vicinity of the true location c_a, then, the estimate error variance is characterized in terms of β_{ik}, the second partial derivative of the ambiguity function evaluated at the origin.

In practice, evaluation of β_{ik} by taking two derivatives of the ambiguity function is tedious, particularly for a discontinuous object $f_o(x)$, since both the integrand and the limits of integration with respect to t in (21) depend on ϵ. The following analysis makes use of frequency domain analysis of the critical operations of interest in tomography (the Radon transform, convolution, and the back-projection) to develop an expression for β_{ik} which is evaluated more easily than the expression in (33).

Evaluating β_{ik}

Letting $F_2^{-1}\{\cdot\}$ denote the 2D inverse Fourier transform [15], and using capital letters ~~to denote Fourier transforms, where the vector $\omega = (\omega_1\ \omega_2)'$ represents a point in the~~ spatial frequency domain,

$$a(\epsilon) = F_2^{-1}\{A(\omega)\} = \int\limits_{-\infty}^{\infty}\int\limits_{-\infty}^{\infty} A(\omega_1,\omega_2)\, e^{j2\pi(\omega_1\epsilon_1 + \omega_2\epsilon_2)}\, d\omega_1\, d\omega_2 \qquad (34)$$

By taking partial derivatives of both sides, β_{ik} may be obtained in terms of $A(\omega)$, the 2D Fourier transform of the ambiguity function $a(\epsilon)$

$$\beta_{ik} = -4\pi^2 F_2^{-1}\{\omega_i\,\omega_k\,A(\omega)\}_{\epsilon=0} \qquad i,k\in\{1,2\} \qquad (35)$$

In a moment, an expression is developed for the Fourier transform of the ambiguity function as a product of several 2D Fourier transforms. First, note that the ambiguity function $a(\epsilon)$ may be written as

$$a(\epsilon) = B(Rf * h * R\tilde{f} * h * \xi) \qquad (36)$$

where $*$ denotes 1D convolution in the t variable in Radon space, $f(x) = d\cdot f_0(x)$ is the object situated at the origin with contrast d, $h(t)$ is the measurement aperture, $\tilde{f}(x_1,x_2) \triangleq f(-x_1,-x_2)$, and B and R are the back-projection and Radon transform operators discussed in Section II. In this expression, the Radon-space function $\xi(t,\theta)$ ~~is a sampling function~~ that allows the limited-view CBP, with an integral over the interval $\theta\in[\frac{\pi}{2}-\Delta,\frac{\pi}{2}+\Delta)$, to be written as a CBP over the continuous interval $0<\theta\leq\pi$.

Claim 1: In the continuous-view measurement case, ξ in (36) is given by

$$\xi_\Delta(t,\theta) = \delta(t)\cdot\mathrm{rect}\left|\frac{\pi-2\theta}{4\Delta}\right| \qquad 0<\Delta\leq\frac{\pi}{2} \qquad (37)$$

where

$$\mathrm{rect}(\tau) = \begin{cases} 1 & \text{if } |\tau|\leq\frac{1}{2} \\ 0 & \text{otherwise} \end{cases} \qquad (38)$$

The function $\xi_\Delta:Y\to R$ in (37) is a truncated impulse sheet in Radon space, that is, it is the product of an impulse sheet along the θ axis and a 2D function that is zero everywhere except for $\theta\in[\frac{\pi}{2}-\Delta,\frac{\pi}{2}+\Delta)$, where it equals unity.

Proof: See Appendix 1.

Since the ambiguity function may be written as the CBP shown in (36), its Fourier transform $A(\omega)$ in (35) may be obtained by using the fact that CBP may be written as a 2D convolution (Davison and Grunbaum [19], Tuy [20]). In particular, letting $F(\omega)$ ~~denote~~ the 2D Fourier transform of $f(x) = d\cdot f_0(x)$, it is shown in Appendix 2 that

$$A(\omega) = |F(\omega)|^2 R_h^2(\omega) B_\xi(\omega) \tag{39}$$

Here $B_\xi(\omega)$ is the 2D Fourier transform of $b_\xi(x)$, the back-projection of the Radon-space function $\xi(t,\theta)$. In (39), $R_h(\omega)$, due to the measurement aperture $h(t)$, is a circularly-symmetric function (since $h(t)$ is θ-independent) with a central section given by $H(\omega)$, the 1D Fourier transform of $h(t)$. The 2D inverse Fourier transform of $R_h(\omega)$ will be denoted as $r_h(x)$. The relationships in (36) and (39) are illustrated schematically in Figure 4.

Combining (35) and (39), the second partial derivative of the ambiguity function $a(\epsilon)$ evaluated at the origin, is given by

$$\beta_{ik} = -4\pi^2 F_2^{-1} \{ \omega_i \omega_k |F(\omega)|^2 R_h^2(\omega) B_\xi(\omega) \}_{\epsilon=0} \qquad i,k \in \{1,2\} \tag{40}$$

The back-projection $b_\xi(x)$ and its 2D Fourier transform

The back-projection of the truncated impulse sheet $\xi_\Delta(t,\theta)$ is derived in Appendix 1, and is given by

$$b_{\xi,\Delta}(x) = \begin{cases} \dfrac{1}{\|x\|} & \text{if } |\phi| \leq \Delta \\ 0 & \text{otherwise} \end{cases} \tag{41}$$

where ϕ is the angular polar coordinate of x, $\phi \in [-\frac{\pi}{2}, \frac{\pi}{2})$. The region of the x-plane where $b_{\xi,\Delta}(x)$ is positive is indicated in Figure 5a. In the special case of full-view measurements, where $\Delta = \frac{\pi}{2}$ the back-projection of $\xi_{\frac{\pi}{2}}$ is positive everywhere and is given by the function $\dfrac{1}{\|x\|}$.

The 2D Fourier transform of $b_{\xi,\Delta}(x)$ is also derived in Appendix 1, and is given by

$$B_{\xi,\Delta}(\omega) = \begin{cases} \dfrac{1}{\|\omega\|} & \text{if } |\psi - \frac{\pi}{2}| \leq \Delta \\ 0 & \text{otherwise} \end{cases} \tag{42}$$

where ψ is the angular polar coordinate of ω, $\psi \in [0,\pi)$. The subset of the ω-plane where $B_{\xi,\Delta}(\omega)$ is positive is shown in Figure 5b; in the full-view case, it is positive everywhere and equals $\dfrac{1}{\|\omega\|}$.[3]

Summarizing, an expression is given in (30) for the ML location estimate error covariance as a linear combination of conditional error covariances. The probabilities p_j in this expression are computed from (27) or some approximation thereof, and the

---

3. In the discrete-view measurement case, ξ in (36) is a train of N two-dimensional impulses uniformly spaced on the interval $[0,\pi)$ along the θ axis in Y. The back-projection $b_\xi(x)$ and its Fourier transform $B_\xi(\omega)$, in this case, are both *spoke functions* [6,14].

conditional error covariances are approximated by (29) when $j \neq 0$, and bounded as shown in (31) when $j = 0$, where the Fisher's information matrix entries in (33) are obtained using the inverse Fourier transform shown in (40). Prior to evaluating these expressions, the regions $C_j \subset C$ and points $\gamma_j \in C_j$ must be chosen appropriately. In the next section, the constant-density disk object in Example 1 is reconsidered; systematic use of the performance analysis machinery just developed is demonstrated through this example. In particular, the ambiguity function for the object localization problem is evaluated, the regions C_j and points γ_j are selected based on an examination of this function, and an approximation to the estimate error covariance Λ_e is evaluated for several different measurement noise levels and different values of object radius. As will be demonstrated, localization performance is characterized by a clear threshold effect; in particular, it is possible to identify, for a given object contrast and a given measurement noise level, the smallest object size that can be located reliably.

In closing, it should be noted that the problem of detecting a constant density disk object having *known location* by examining a reconstructed image has been considered by Hanson [6], who empirically identified the relationship between minimum detectable contrast and object diameter. It is well known [16] that when the noise in projection measurements is white, the noise in the reconstructed image is nonwhite. Hanson demonstrated the necessity of appropriate 2D filtering of the reconstructed imagery; without such filtering, human interpreters have difficulty in detecting large low contrast objects in the presence of colored reconstruction noise. The "appropriate" 2D filter essentially corresponds to a whitening filter [13], which undoes the noise correlating effect of the CBP operation.

IV. EXAMPLE

Reconsider Example 1 in Section II, involving a constant-density object on a disk of radius R centered at the point $c_a \in C \subset R^2$, and suppose that the set C of possible object locations is itself a disk of radius T

$$C = \{ x : \|x\| \leq T \} \tag{43}$$

Since many of the expressions in this section will depend on T and R only through their ratio, the parameter k is defined

$$k \triangleq T/R \tag{44}$$

When the object is located at the origin, its density function is given by

$$d \cdot f_0(x) = \begin{cases} d & \text{if } \|x\| \leq R \\ 0 & \text{otherwise} \end{cases} \tag{45}$$

This density function is circularly symmetric and consequently its 2D Fourier transform is also circularly symmetric [15]. Letting $f(r)$ and $F(\rho)$ denote the density function in (45) and its 2D Fourier transform as functions of their radial polar coordinate only,

$$f(r) = d \cdot \text{rect}(r/2R) \tag{46}$$

where rect(t) is defined in (38), and $F(\rho)$, known as the Fourier-Bessel or Hankel transform of order zero of $f(r)$ [15] is given by

$$F(\rho) = 2\pi \int_0^\pi f(r) J_0(2\pi r \rho)\, r\, dr = (Rd/\rho) J_1(2\pi R \rho) \tag{47}$$

Here, $J_0(\cdot)$ and $J_1(\cdot)$ are Bessel functions of the first kind of order zero and one respectively.

In this example, the full-view measurement case is considered -- the measurements are noisy projections that are bandlimited, i.e. smoothed by 2W times the sinc aperture in (5). The 1D Fourier transform of h(t) is

$$H(\omega) = \text{rect}(\omega/2W) \tag{48}$$

In the full-view case being considered,

$$B_{\xi,\Delta}(\omega) = \frac{1}{\|\omega\|} \tag{49}$$

The ambiguity function and its 2D Fourier transform in (39) are both circularly symmetric. Denoting them respectively by $a(r)$ and $A(\rho)$ as functions of their radial polar coordinates only, $a(r)$ may be expressed in terms of the inverse Hankel transform [15] as

$$a(r) = 2\pi \int_0^\infty A(\rho) J_0(2\pi r \rho)\, \rho\, d\rho \tag{50}$$

From (39), (47)-(49) and a change of variable,

$$a(r) = 2\pi d^2 R^3 \int_0^{RW} J_1^2(2\pi\rho) J_0(2\pi\rho r/R)(1/\rho^2)\, d\rho \triangleq E\, a^*(r/R, RW) \tag{51}$$

where E is the energy in the Radon transform (i.e. the signal part of the measurements),

$$E \triangleq \int_0^\pi \int_{-R}^R \left\{ 2d\sqrt{R^2 - t^2} \right\}^2 dt\, d\theta = \frac{16}{3}\pi d^2 R^3 \tag{52}$$

The normalized ambiguity function a^* is seen to depend on the spatial bandwidth W only through the radius-bandwidth product RW; a^* is plotted in Figure 6 for several values of RW. The radius-bandwidth product has a simple interpretation; it equals the object radius R, expressed as a number of wavelengths at frequency W. As Figure 6 indicates, the general shape of the location ambiguity function is virtually independent of the value of radius-bandwidth product for values of RW in excess of 0.5, i.e. whenever the object diameter exceeds one wavelength at frequency W. In this example, performance is analyzed for radius-bandwidth products in excess of 0.5.

As was discussed in Section III, an approximation to the error covariance of the location estimate may be obtained by partitioning the parameter space C into M non-overlapping regions C_j, and then evaluating the linear combination of conditional error

covariances in (30), where γ_j is a point in C_j. In this example, C is a disk of radius T, and it is partitioned into square regions of side length 2R, centered at the points

$$\gamma_j \in \{(2Rm,2Rn): (2Rm,2Rn) \in C, \text{ m,n integer}\} \tag{53}$$

This value of region size, although somewhat arbitrarily chosen, appears to be appropriate in view of the discussion in Section III and the form of the ambiguity function in Figure 6 for $RW > 0.5$. In particular, each region C_j is small enough so that the log likelihood function $L(\epsilon)$ can, for the purposes of global error analysis, be reasonably approximated by a piecewise constant function on regions C_j, yet large enough so that the statistical correlation between random variables L_i and L_j, $i \neq j$ is small enough to allow an easy approximation to the probabilities p_j in (27), as is discussed shortly.

When the regions C_j are squares with side length 2R, the number of regions in the disk C is approximately the ratio of the disk area πT^2 to the region area $4R^2$, or using k in (44),

$$M \approx \frac{\pi T^2}{4R^2} = \frac{\pi}{4}k^2 \tag{54}$$

To proceed with evaluation of the approximate error covariance in (30), the probabilities p_j in (27) and the conditional error covariance Λ_0 are needed. Considering the first of these, the set of random variables $L_j = L(\gamma_j)$, $j = 0,1,...,M-1$ are jointly Gaussian and as indicated by (26) and Figure 6, have nonzero mean and nonzero covariance. Because the log likelihood function values L_j are correlated, determination of the probabilities p_j in (27) is computationally intensive, involving an M-dimensional numerical integration if evaluated directly. The analysis in this example will exploit the fact that the coefficient of correlation between L_i and L_j,

$$\lambda_{ij} = \frac{E\left[(L_i - E\{L_i\})(L_j - E\{L_j\})\right]}{\left[E\left[(L_i - E\{L_i\})^2\right] E\left[(L_j - E\{L_j\})^2\right]\right]^{1/2}} = \frac{1}{E}a(\gamma_i - \gamma_j) \tag{55}$$

is always less than 0.35, for $i \neq j$. This correlation is neglected, and the random variables L_i and L_j are approximated as being uncorrelated when $i \neq j$. This is equivalent to assuming that the ambiguity function equals zero for $|\frac{r}{R}| \geq 2$.

The error introduced by this approximation is minor, and in fact, this approximation makes the results conservative in the following sense. When the L_j are approximated as being uncorrelated, and conditioned on $c_a = \gamma_0$, the probability masses at the points γ_j are identical for $j = 1,2,...,M-1$. That is, conditioned on the peak lying in an incorrect region, under this approximation it is equally likely to occur in *any* one of the regions $C_1, C_2, \ldots, C_{M-1}$, and

$$p_j = \frac{1 - p_0}{M - 1} \qquad j = 1,2, \ldots, M-1 \tag{56}$$

Actually, however, since the ambiguity function is positive and monotonically

decreasing away from the point c_a, if the peak lies in an incorrect region, it will be more likely to lie close to the location of the true object, rather than far away.

Under the approximation of uncorrelated L_j, a simple approximation for the probabilities p_j in (27) may be obtained. If the true object location c_a is γ_0, then the union bound [13] may be used to approximate the probability of error, $1 - p_0$, as

$$\text{Prob(error)} = 1 - p_0 = 1 - \text{Prob}\{L_0 > L_j, \ \forall j \neq 0\}$$

$$\approx \frac{M-1}{\sqrt{2\pi E/N_o}} \exp\left(-\frac{E}{2N_o}\right) \tag{57}$$

While the last line is an upper bound on the error probabilty, it is tight for values of E/N_o in excess of five or so [13]; since the performance is assessed for SNR values greater than five in this example, the expression in (57) is treated as an *accurate approximation* to the error probabilty, rather than as a bound.

Using (56), the approximate error covariance in (30) becomes

$$\Lambda_e \approx \Lambda_0 p_0 + (1 - p_0) \sum_{j=1}^{M-1} \left[\frac{1}{M-1}\right] (\gamma_j - \gamma_0)(\gamma_j - \gamma_0)' \tag{58}$$

The (M-1)-term summation corresponds to the second moment about the point γ_0 of a discrete 2D random variable which is equally likely to occur at any one of M-1 points on the lattice

$$\{(2Rm, 2Rn): (2Rm, 2Rn) \in C, \ m,n \text{ integer, not both zero}\} \tag{59}$$

This moment is well approximated by considering a 2D continuous random variable uniformly distributed on the disk C; it has a second moment about the point $\gamma_0 = c_a$ of

$$\begin{bmatrix} T^2/4 + c_{a1}^2 & c_{a1} c_{a2} \\ c_{a1} c_{a2} & T^2/4 + c_{a2}^2 \end{bmatrix} \tag{60}$$

where $c_a = (c_{a1} \ c_{a2})'$. For the sake of illustration, only the case where the object is located at the origin is considered here, in which case (58) becomes

$$\Lambda_e \approx \Lambda_0 p_0 + (1 - p_0)(T^2/4) I \tag{61}$$

where I is the 2×2 identity matrix.

The final step in the performance characterization is the local error analysis involving computation of the 2×2 Fisher's information matrix J. From (33), the ik^{th} entry in the Fisher's information matrix is $-\frac{2}{N_o}\beta_{ik}$, where from (40), (42), (47) and a change to polar coordinates (ρ, ψ),

$$\beta_{ik} = -(2\pi Rd)^2 \int_0^\pi \nu(\psi) d\psi \int_{-\infty}^\infty J_1^2(2\pi R|\rho|) H^2(\rho) d\rho \tag{62}$$

where

$$\nu(\psi) = \begin{cases} \cos^2\psi & \text{if } i=k=1 \\ \sin^2\psi & \text{if } i=k=2 \\ \cos\psi\,\sin\psi & \text{if } i\neq k \end{cases} \tag{63}$$

Performing the integration with respect to $\psi, \beta_{12} = \beta_{21} = 0$, and

$$\beta_{ii} = -2R(\pi d)^2 \int_0^{2\pi RW} J_1^2(\rho)\,d\rho \overset{\Delta}{=} -(3\pi/8R^2)E\,\mu(RW) \qquad i\in\{1,2\} \tag{64}$$

where E is the Radon transform energy given in (52). By the symmetry of the problem, then, the Fisher's information matrix is a scalar times the 2×2 identity matrix, and from (31) the diagonal entries of the conditional error covariance Λ_0 are bounded by

$$\left[\Lambda_0\right]_{ii} \geq -\frac{N_0}{2\beta_{ii}} \qquad i\in\{1,2\} \tag{65}$$

A plot of the function $\mu(RW)$ in (64) for $RW \in [0,10)$ is shown in Figure 7. Note that $\mu(RW)$ is a monotonically nondecreasing function and as RW approaches infinity (i.e. for a fixed object size R, as the measurement system bandwidth W approaches infinity), $\mu(RW)$ becomes infinite. This implies that the ambiguity function $a(r)$ is not twice differentiable in the limit $RW\to\infty$ ($s(t,\theta)$ approaches a half-ellipse which has points of infinite first derivative), and the Cramer-Rao lower bound in (65) degenerates to zero. This is a well-known phenomemon that also arises in radar performance analysis in the limiting case of infinite measurement system bandwidth [21]. In any practical case, smoothing or bandlimiting of the projection measurements always occurs, so that the aperture $h(t)$ is nonimpulsive and the radius-bandwidth product is finite.

Denoting by σ_e^2 the diagonal entries in the approximation to Λ_e in (30), it follows from (60) that

$$\sigma_e^2 \geq -\frac{N_0}{2\beta_{ii}}p_0 + (1-p_0)\frac{T^2}{4} = -\frac{N_0}{2\beta_{ii}} + \left[\frac{T^2}{4} + \frac{N_0}{2\beta_{ii}}\right](1-p_0) \tag{66}$$

Finally, by incorporating the approximation for $(1-p_0)$ in (57), approximating M-1 as shown in (54), and using (64), the error covariance σ_e^2 normalized by T^2, is approximately lower bounded by the following quantity

$$\left[\frac{\sigma_{LB}}{T}\right]^2 = \frac{4}{3\pi k^2(E/N_0)\mu(RW)} +$$

$$\left[\frac{1}{4} - \frac{4}{3\pi k^2(E/N_0)\mu(RW)}\right]\frac{\pi k^2}{4\sqrt{2\pi E/N_0}}\exp\left(-\frac{E}{2N_0}\right) \tag{67}$$

The dependence of the localization performance on the object size R, for a fixed value of density, may be illustrated by substituting E from (52) and considering (67) for fixed values of d^2/N_0. The inverse of this normalized error variance is plotted in Figure 8 versus normalized object size R/T for three values of $d^2/N_0 = 60, 500$ and 7500, with $W = 50$. These curves depict a very strong threshold behavior in localization performance; for a given object contrast d and noise level N_0, there exists a clearly defined smallest sized object that can be located reliably from noisy projection data.

Summarizing, the analysis of this section has focused on the problem of using noisy, full-view projection measurements of a cross-section to estimate the location of a constant-density disk object. A framework has been presented for evaluating the estimation performance. Quantitative performance analyses may also be carried out within this framework for the cases of limited-view $(\Delta < \frac{\pi}{2})$ and discrete-view projection measurements, as well as for other object models, such as the Gaussian object mentioned in Section II [14].

V. COMPUTER SIMULATION

A limited amount of noisy projection data were generated by computer and were processed using a CBP algorithm for two purposes, (1) to determine the 2D log likelihood function for the unknown object location and (2) by using a conventional reconstruction kernel, to develop an estimate for the 2D cross-sectional density function.

The specific example considered in these simulations is the simple disk object of Example 1, having radius R and situated at within the disk C of radius T. The object size is chosen so that $k = T/R$ in (44) equals 5. For notational convenience, the geometry is normalized so that T equals unity, in which case the object has a radius $R = 0.2$. The actual object is located at the point (0.2, 0.4); an image representation of this cross-section is shown in Figure 9.

A total of 105 projection measurements were calculated, corresponding to infinitely narrow line integral measurements $(RW = \infty)$ using a parallel-ray measurement geometry. Five views were generated at angles $\theta_j = j\pi/5, j = 0,1, \ldots, 4$. Within each view, integrals were calculated along 21 parallel lines with t values satisfying $t_m = 0.1m, m = -10, -9, \ldots, 10$, corresponding to an inter-ray spacing of 0.1.

Pseudorandom white noise samples having zero mean and adjustable variance σ^2 were added to the 105 line integrals to provide noisy measurements $y(t_m, \theta_j)$. The measurement signal-to-noise ratio (SNR) in dB is defined as

$$\text{SNR} \triangleq 10 \log_{10} (E_d/105\,\sigma^2) \tag{68}$$

where E_d is the Radon transform energy

$$E_d = \sum_{j=0}^{4} \sum_{m=-10}^{10} g^2(t_m, \theta_j) \tag{69}$$

and $g(t,\theta)$ is the Radon transform of the simulated density function.

The noisy data $y(t_m, \theta_j)$ were processed to develop 240×240 pixel images (16 grey levels per pixel) by using the CBP equation

$$a(\mathbf{x}) = \sum_{j=0}^{4} \sum_{m=-10}^{10} y(t_m, \theta_j) \, z(t_m - \mathbf{x}'\theta_j, \theta_j) \qquad |x_1|, |x_2| \leq 1 \tag{70}$$

The convolving kernel $z(t,\theta)$ is given by one of two functions, depending on whether the log likelihood function or a reconstructed image is being computed. In each case, a piecewise linear approximation to the ideal continuous convolving kernel was used in order to reduce the computation time.

Since the disk object is circularly-symmetric, the convolving kernel for the log likelihood function evaluation, denoted by $z_{LL}(t)$, is θ-independent, and is given by the following piecewise linear approximation to the projection of a disk with a radius of 0.2.

$$z_{LL}(t) = \begin{cases} 2\sqrt{(0.2)^2 - t^2} & \text{if } |t| \leq 0.2, \ t \text{ an integer multiple of } 0.02 \\ 0 & \text{if } |t| > 0.2, \ t \text{ an integer multiple of } 0.02 \end{cases} \tag{71}$$

If t is not an integer multiple of .02, the value of $z_{LL}(t)$ is obtained by linear interpolation of its two nearest values in (71).

In calculating a reconstructed image, the convolving kernel, denoted $z_I(t)$, is the θ-independent kernel presented in Shepp and Logan [1], and is given by the piecewise linear function

$$z_I(t) = \frac{1}{10\pi} \frac{1}{0.25 - 100t^2} \qquad \text{if } t \text{ is an integer multiple of } 0.1 \tag{72}$$

If t is not an integer multiple of 0.1, the value of $z_I(t)$ is obtained by linear interpolation of its two nearest values in (72).

In this simulation, two measurement SNR noise levels (68) were used, namely 0 dB and -3 dB, and the same noise samples at each level were used with both convolving kernels. To simplify interpretation of the images, the image values are first normalized to the interval [0,1] with 0 and 1 corresponding to black and white, respectively, and the 16-level gray scale is then uniformly distributed on the interval [.6,1] or [.75,1] as indicated, resulting in the blackening out of lower intensity regions.

Figures 10a and 10b correspond to the log likelihood function (kernel in (71)) and reconstructed image (kernel in (72)), respectively, when the measurement SNR is 0 dB and the gray scale is distributed on the interval [.6,1]. Figures 10c and 10d are the log likelihood function and reconstructed image for a SNR equal to -3 dB, and the gray scale distributed on the interval [.75,1]. Notice that for both measurement noise levels the image reconstruction kernel $z_I(t)$, because of its higher gain at high frequencies, leads to spurious peaks in the reconstruction, all having approximately the same size and distributed throughout the cross-section. The log likelihood

function, on the other hand, has only one peak in the 0 dB case, occurring at (0.24, 0.34), which is very close to the true object location (0.2, 0.4). In the -3 dB case, the log likelihood function has several secondary peaks, but the major peak, located at (0.18, 0.49), is also close to the true location.

As indicated by Figures 10b and 10d, object detection and localization is difficult by direct visual examination of noisy reconstructed imagery. As discussed at the end of Section III, image post-processing to extract object related information has been considered by Hanson [6] and others. In the presence of projection measurement noise that is white, the reconstructed image noise is nonwhite [16], in which case optimal object localization from reconstructed imagery involves 2D noise pre-whitening followed by matched filtering. A suboptimal approach to post-processing a reconstructed image for object identification purposes, and one that is quite often used in image processing, is to perform matched filtering assuming that the measurement noise is white. For the present problem, this corresponds to performing 2D matched filtering on the reconstructed image using a disk object template.

The reconstructed images in Figures 10b and 10d were post-processed by treating the reconstructed image noise as white, and performing matched filtering to locate a constant-density object of radius 0.2. The following 2D matched filter template was used

$$f_c(x) = \begin{cases} 1 & \text{if } |x| \le 0.2 \\ 0 & \text{otherwise} \end{cases} \tag{73}$$

The image in Figure 11a is the result of matched filtering the image in Figure 10b with $f_c(x)$, with the gray scale distributed on [.6,1]. Similarly, Figure 11b is the result of matched filtering the image in Figure 10d, with the gray scale distributed on [.75,1]. These two images are seen to be very similar to the log likelihood images in Figures 10a and 10c, although the log likelihood images were computed directly in much less time than the two-step process of first reconstructing and then performing 2D matched filtering. The similarity of these images is due in part to the robustness of the matched filter -- even though the matched filter in (73) is optimal only in the presence of white image noise, its performance is very robust to the presence of nonwhite noise.

VI. CONCLUSIONS

In this paper the problem has been investigated of using ML estimation methods in order to locate a single object whose geometry is known precisely a priori. An approximate expression was developed in Section III for the location estimate error covariance, reflecting contributions due to both local and global errors. In Section IV, an approximation to this expression was evaluated for a constant-density disk object; the results of this example indicate that for a given value of object contrast d and noise spectral level N_o, there exists a minimum value of object size for which reliable localization may be performed.

A computer simulation was also presented which illustrates the evaluation of the log likelihood function for the localization of a constant-density disk object from computer-generated noisy projections, as well as the evaluation of a reconstructed

image from the same noisy measurements. These simulations demonstrate that at high noise levels and with a limited number of projections, an object in a cross-section is much more easily discerned by examining the log likelihood function than by examining a reconstructed image that has not undergone time-consuming post-processing.

The focus of Part I was the simple problem of locating a single object of known contrast and density distribution $f_0(x)$, superimposed on a *known* background field that contains no additional objects. By casting the problem in this framework, insight was obtained about the CBP computational structure of the log likelihood function evaluation, and the peformance of the ML estimator was characterized. In Part II, robustness issues are addressed, in particular, the robustness of these procedures when applied to less idealized versions of the problem that take into account, for example, that the object size, shape, or detailed density variations may differ from those that are assumed, or that additional unmodeled objects may be present within the cross-section.

APPENDIX 1 -- Radon Space Sampling Function $\xi_\Delta(t,\theta)$

Proof of Claim 1:

From (21) and (23), the continuous-view ambiguity function is

$$a_\Delta(\epsilon) = \int_{\frac{\pi}{2}-\Delta}^{\frac{\pi}{2}+\Delta} \int_{-\infty}^{\infty} s(t,\theta) \, s(t-\epsilon'\theta,\theta) \, dt \, d\theta$$

$$= \int_0^\pi \text{rect}\left[\frac{\pi-2\theta}{4\Delta}\right] \int_{-\infty}^{\infty} s(t,\theta) \, s(t-\epsilon'\theta,\theta) \, dt \, d\theta = B\left\{\text{rect}\left[\frac{\pi-2\theta}{4\Delta}\right] \cdot (s * \tilde{s})\right\}$$

where $\tilde{s}(t,\theta) \triangleq s(-t,\theta)$ and B is the back-projection operator defined in (20).

$$a_\Delta(\epsilon) = B\left\{ s * \int_{-\infty}^{\infty} \tilde{s}(\tau,\theta) \, \delta(t-\tau) \, \text{rect}\left[\frac{\pi-2\theta}{4\Delta}\right] d\tau \right\}$$

$$= B\left\{ s * \int_{-\infty}^{\infty} \tilde{s}(\tau,\theta) \, \xi_\Delta(t-\tau,\theta) \, d\tau \right\} = B\left\{ s * \tilde{s} * \xi_\Delta \right\} \tag{A1.1}$$

which agrees with (36), since $s = Rf * h$ by (4).

Back-projection of $\xi_\Delta(t,\theta)$ [1]

From the definition of the back-projection operator in (20), the back-projection of the truncated impulse sheet $\xi_\Delta(t,\theta)$ in (37) is given by

$$b_{\xi,\Delta}(x) = \int_0^\pi \xi_\Delta(x'\theta,\theta) \, d\theta = \int_0^\pi \delta(x'\theta) \, \text{rect}\left[\frac{\pi-2\theta}{4\Delta}\right] d\theta$$

$$= \int_{\frac{\pi}{2}-\Delta}^{\frac{\pi}{2}+\Delta} \delta(x'\theta) \, d\theta = \int_{\frac{\pi}{2}-\Delta}^{\frac{\pi}{2}+\Delta} \delta(r\cos(\theta-\phi) \, d\theta \tag{A1.2}$$

where (r,ϕ) are the polar coordinates of x, $r \in (-\infty,\infty)$, and $\phi \in [-\frac{\pi}{2},\frac{\pi}{2})$. By a change of variable

$$b_{\xi,\Delta}(x) = \int_{r\cos(\frac{\pi}{2}-\phi-\Delta)}^{r\cos(\frac{\pi}{2}-\phi+\Delta)} \frac{\delta(\tau) \, d\tau}{\sqrt{r^2-\tau^2}} \tag{A1.3}$$

---

1. For an alternative derivation of the limited-view impulse response function, see Tuy [20].

which provides

$$
b_{\xi,\Delta}(\mathbf{x}) = \begin{cases} \dfrac{1}{\|\mathbf{x}\|} & \text{if } |\phi| \leq \Delta \\ 0 & \text{otherwise} \end{cases} \tag{A1.4}
$$

Fourier Transform of $b_{\xi,\Delta}(\mathbf{x})$

The 2D Fourier transform of $b_{\xi,\Delta}(\mathbf{x})$ in (A1.4) is given in terms of the polar coordinates (r,ϕ) as

$$
\begin{aligned}
B_{\xi,\Delta}(\boldsymbol{\omega}) &= \int_{-\Delta}^{\Delta} \int_{-\infty}^{\infty} \frac{1}{|r|} e^{-j2\pi r(\omega_1\cos\phi \,+\, \omega_2\sin\phi)} \, |r| \, dr \, d\phi \\
&= \int_{-\Delta}^{\Delta} d\phi \int_{-\infty}^{\infty} e^{-j2\pi r\omega'\phi} \, dr
\end{aligned} \tag{A1.5}
$$

where $\phi = (\cos\phi \ \ \sin\phi)'$ and $\boldsymbol{\omega} = (\omega_1 \ \ \omega_2)'$.

The second integral in (A1.5) is the 1D Fourier transform, evaluated at $\omega'\phi$, of a function that is unity for all r. Thus,

$$
B_{\xi,\Delta}(\boldsymbol{\omega}) = \int_{-\Delta}^{\Delta} \delta(\omega'\phi) \, d\phi \tag{A1.6}
$$

Equation (A1.6) has the same form as (A1.2), and by a change of variable yields

$$
B_{\xi,\Delta}(\boldsymbol{\omega}) = \begin{cases} \dfrac{1}{\|\boldsymbol{\omega}\|} & \text{if } |\psi - \frac{\pi}{2}| \leq \Delta \\ 0 & \text{otherwise} \end{cases} \tag{A1.7}
$$

where ψ is the angular polar coordinate of the point $\boldsymbol{\omega}$.

APPENDIX 2 -- Calculating $A(\boldsymbol{\omega})$

In terms of the Radon transform and back-projection operators R and B in (1) and (20), CBP with a θ-dependent convolving kernel $z(t,\theta)$ may be written as

$$
\hat{f}(\mathbf{x}) = \int_{0}^{\pi} \int_{-\infty}^{\infty} g(t,\theta) z(t - \mathbf{x}'\theta,\theta) \, dt \, d\theta = B\,(Rf * \bar{z}) \tag{A2.1}
$$

where $\bar{z}(t,\theta) \triangleq z(-t,\theta)$, and $*$ denotes 1D convolution in t,

$$
[z_1 * z_2](\tau) = \int_{-\infty}^{\infty} z_1(t,\theta) z_2(\tau - t,\theta) \, dt \tag{A2.2}
$$

Letting ** denote 2D convolution, it is shown in Davison and Grunbaum [18] that (A2.1) may be rewritten as

$$B\ (Rf * \tilde{z}) = f ** B\ (\tilde{z}) \tag{A2.3}$$

that is, CBP operating on Rf with a convolving kernel $z(t,\theta)$ may be written as the 2D convolution of $f(x)$ with the back-projection of $\tilde{z}(t,\theta)$.

The relationship in (A2.3) leads to an expression for the Fourier transform of the ambiguity function. In particular, from (36),

$$a(\epsilon) = B\ (Rf * h * R\tilde{f} * h * \xi) \tag{A2.4}$$

Here, $f(x) = d \cdot f_0(x)$ is the object situated at the origin and having contrast d, $\tilde{f}(x_1,x_2) \triangleq f(-x_1,-x_2)$, and ξ is the sampling function given in (37). Denoting by $r_h(x)$ the circularly-symmetric 2D function satisfying $R\ (r_h(x)) = h(t)$ (that is, a central slice of $R_h(\omega)$, the 2D Fourier transform of $r_h(x)$, is given by $H(\omega)$, the 1D Fourier transform of $h(t)$), and successively applying (A2.3),

$$a(\epsilon) = f ** r_h ** \tilde{f} ** r_h ** b_\xi \tag{A2.5}$$

Taking 2D Fourier transforms, and noting that f is real,

$$A(\omega) = |F(\omega)|^2 R_h^2(\omega) B_\xi(\omega) \tag{A2.6}$$

REFERENCES

[1] Shepp, L.A., B.F. Logan. 1974. The Fourier reconstruction of a head section. IEEE Trans. Nucl. Sci. NS-21:21-43.

[2] Mersereau, R.M., A.V. Oppenheim. 1974. Digital reconstruction of multidimensional signals from their projections. Proc. IEEE 62:1319-1338.

[3] Rowland, S.W. 1979. Computer implementation of image reconstruction formulas. Chapter 2 in *Topics in applied physics, Vol 32, Image reconstruction from projections - implemention and applications.* Ed. G.T. Herman. Springer-Verlag, New York.

[4] Klyuev, V.V., E.I. Vainberg, I.A. Kazek and V.P. Kurozaev. 1980. Computational tomography - a new radiation method of nondestructive testing, I, II. Soviet J. Nondestr. Testing 16:180-185,186-193.

[5] Munk, W., C. Wunsch. 1979. Ocean acoustic tomography: a scheme for large scale monitoring. Deep Sea Research 26A:123-161.

[6] Hanson, K.M. 1978. Detectability in the presence of computed tomographic reconstruction noise. Proc. SPIE 127, Medicine VI, 304-312.

[7] Selfridge, P.G., J.M.S. Prewitt. 1981. Organ detection in abdominal computerized tomography scans: application to the kidney. Computer Graphics and Image Proc. 15:265-278.

[8] Glover, G.H., N.J. Pelc, 1981. An algorithm for the reduction of metal clip artifacts in CT reconstructions. Med. Phys. 8:799-807.

[9] Cornuelle, B. 1982. Acoustic tomography. IEEE Trans. Geoscience and Remote Sensing. GE-20:326-332.

[10] Dines, K.A., R.J. Lytle. 1979. Computerized geophysical tomography. Proc. IEEE 67:1065-1073.

[11] Parker, R.L. 1977. Understanding inverse theory. Ann. Rev. Earth Planet. Sci. 5:35-64.

[12] Gordon, R. 1973. Artifacts in reconstructions made from a few projections. Proc. First Int. Joint Conf. on Pattern Recog. 275-285.

[13] Van Trees, H.L. 1968. *Detection, estimation, and modulation theory, Part I, Detection, estimation, and linear modulation theory.* John Wiley and Sons, New York.

[14] Rossi, D. 1982. *Reconstruction from projections based on detection and estimation of objects.* Ph.D. Thesis, Department of Electrical Engineering and Computer Science, M.I.T., 342 p.

[15] Bracewell, R. 1965. *The Fourier transform and its applications.* McGraw-Hill, New York.

[16] Riederer, S.J., N.J. Pelc and D.A. Chesler. 1978. The noise power spectrum in computed x-ray tomography. Phys. Med. Biol. 23:446-454.

[17] Van Trees, H.L. 1971. *Detection, estimation, and modulation theory, Part III, Radar-sonar signal processing and Gaussian signals in noise.* John Wiley and Sons, New York.

[18] Gallager, R.G., C.W. Helstrom. 1969. A bound on the probability that a Gaussian process exceeds a given function. IEEE Trans. Inform. Theory IT-15:163-166.

[19] Davison, M.E., F.A. Grunbaum. 1981. Tomographic reconstruction with arbitrary directions. Comm. in Pure and Appl. Math. 34:77-120.

[20] Tuy, H. 1981. Reconstruction of a 3-dimensional object from a limited range of views. J. Math. Analysis and Appl. 80:598-616.

[21] Skolnik, M.I. 1962. *Introduction to radar systems.* McGraw-Hill, New York.
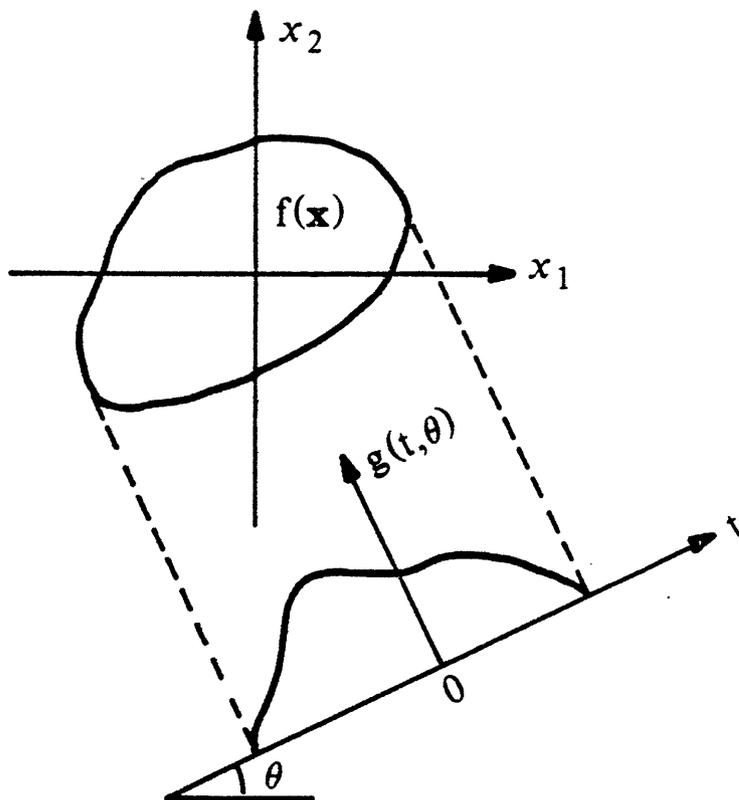
Figure 1. Projection at angle θ.
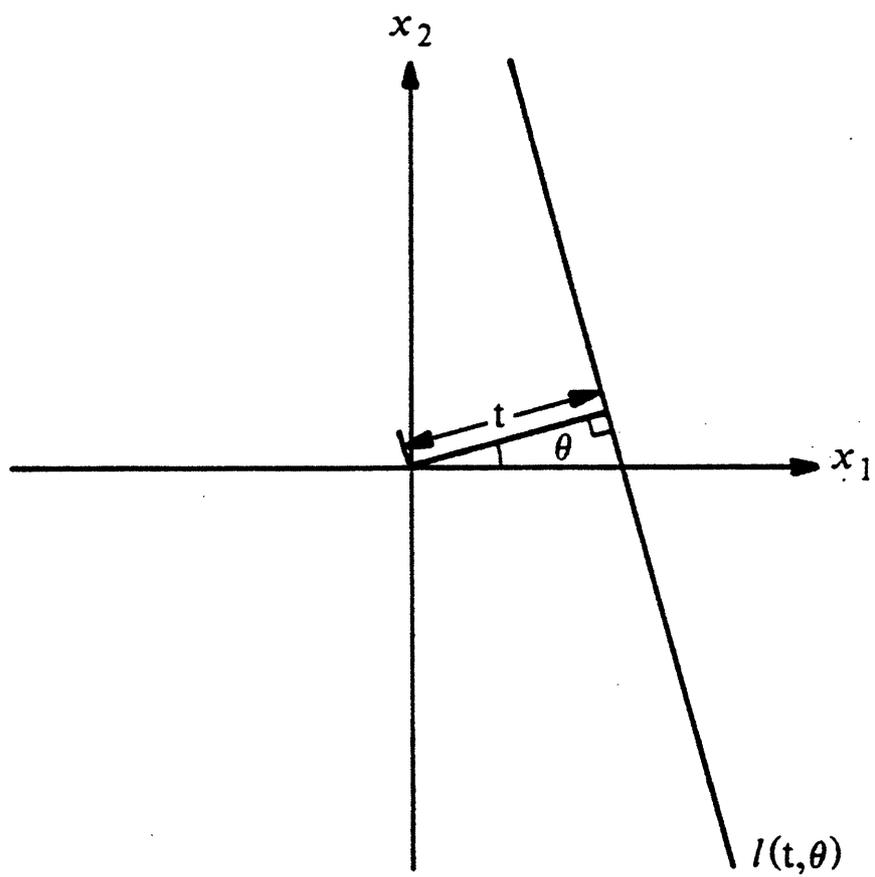
Figure 2. Measurement geometry.
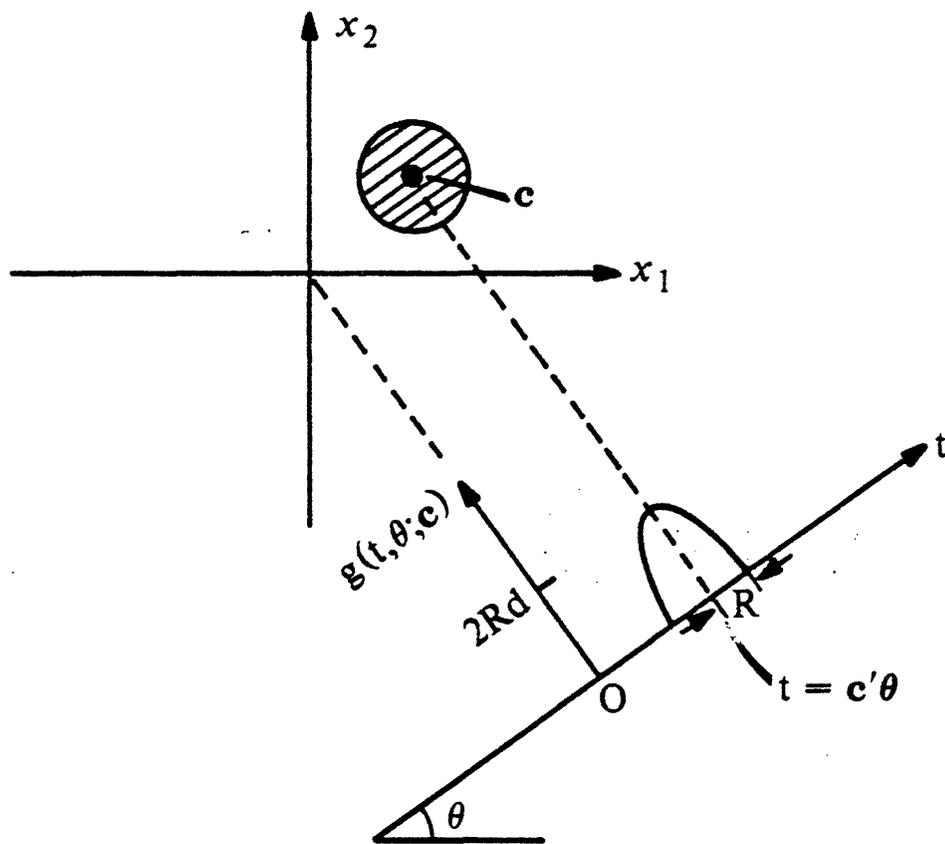
Figure 3(a). Projection of the disk object.
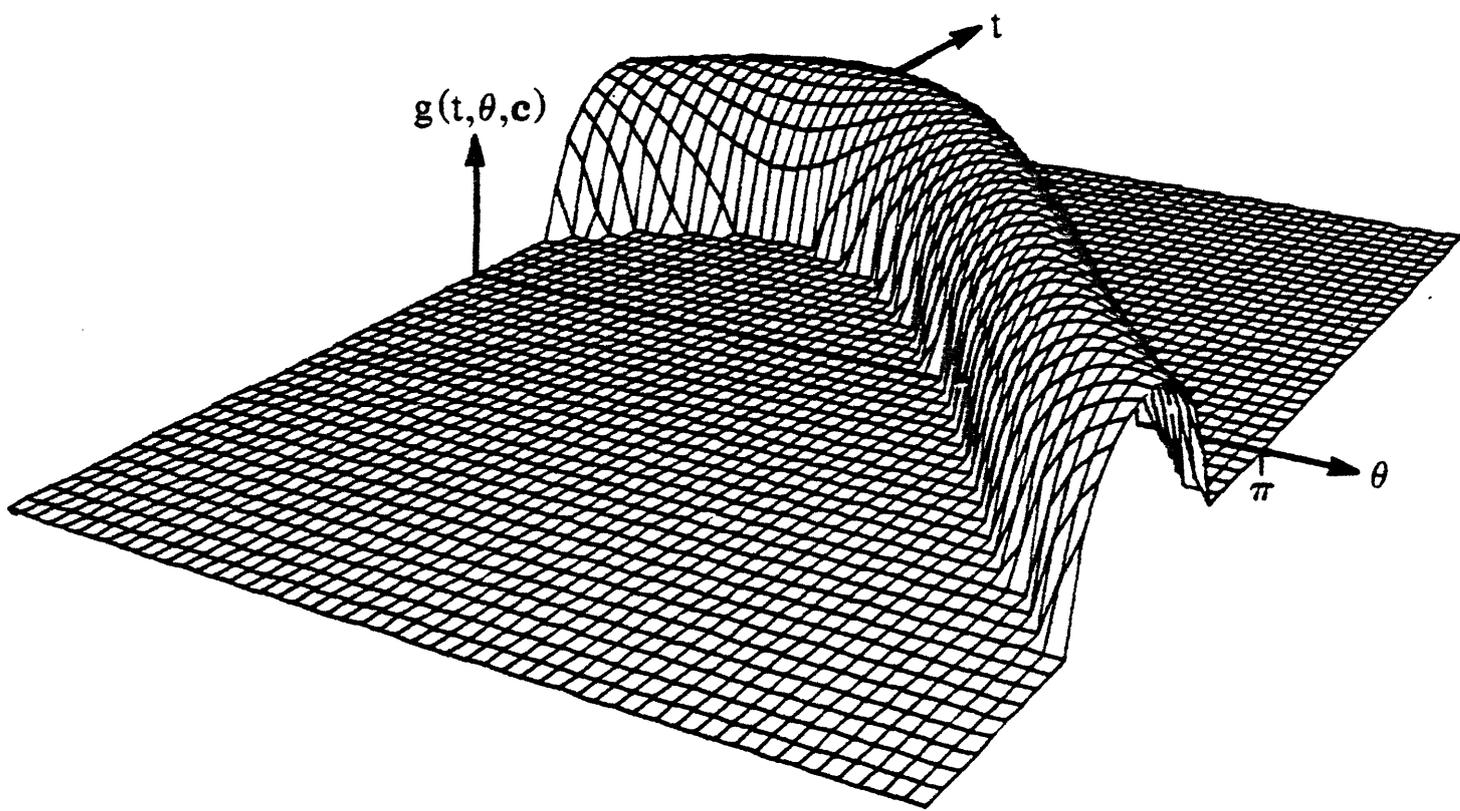
Figure 3(b). Radon transform of the disk object.

$$a(\varepsilon) = B \left[Rf * h * R\tilde{f} * h * \xi \right]$$

$$A(\omega) = F(\omega)\tilde{F}(\omega)R_h^2(\omega)B_\xi(\omega)$$
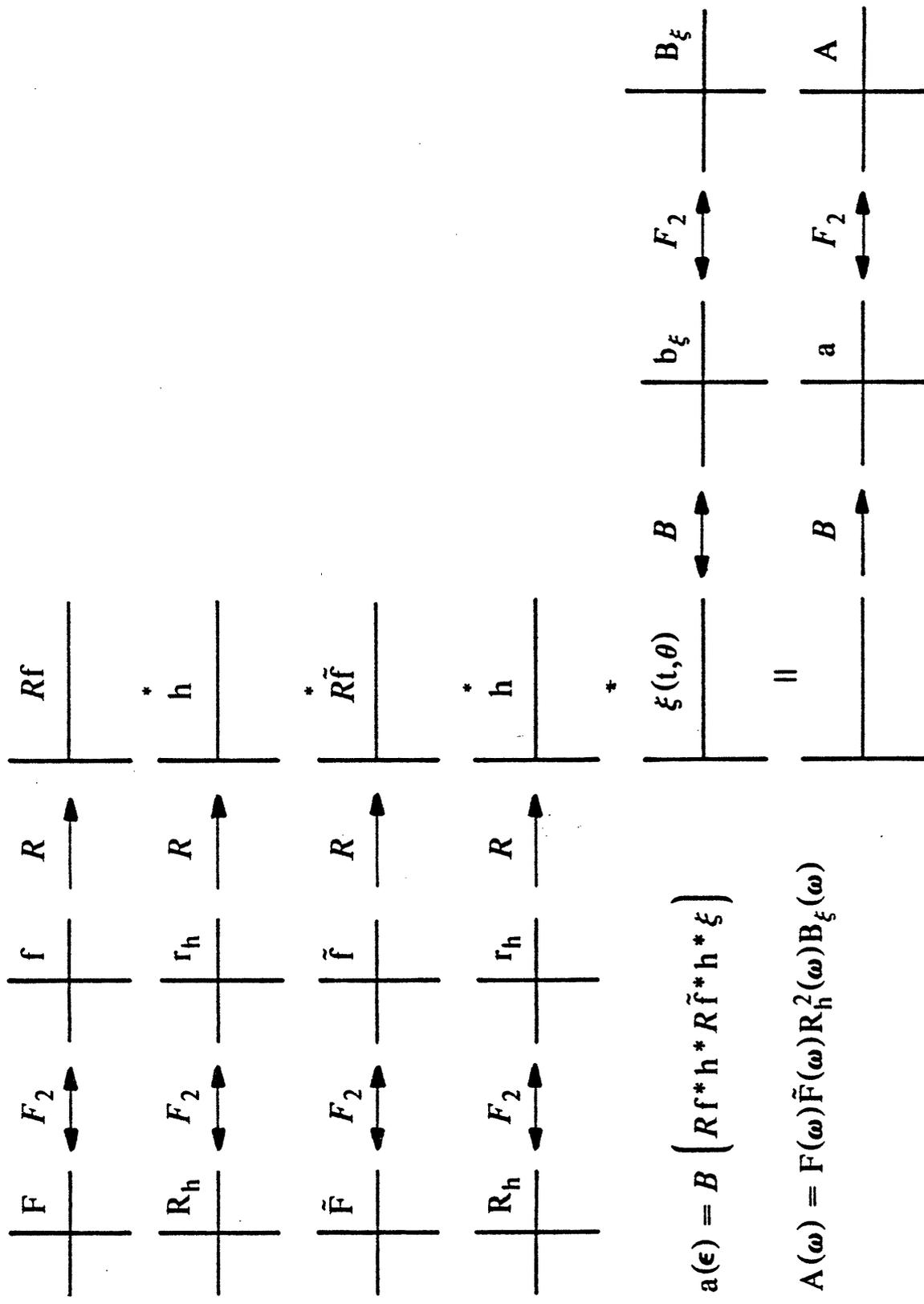
Figure 4. Schematic representation of the transform relationships.
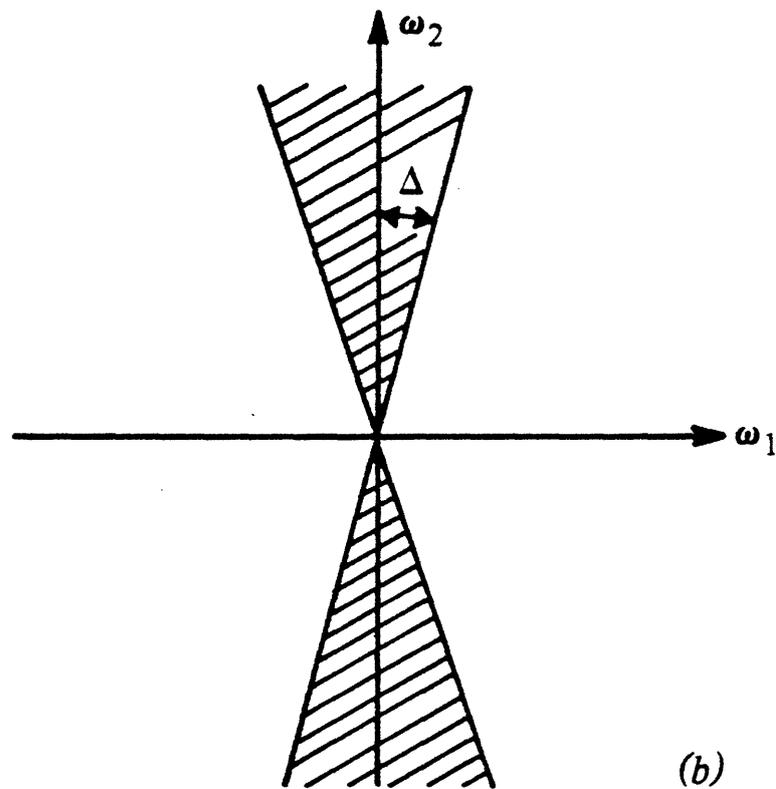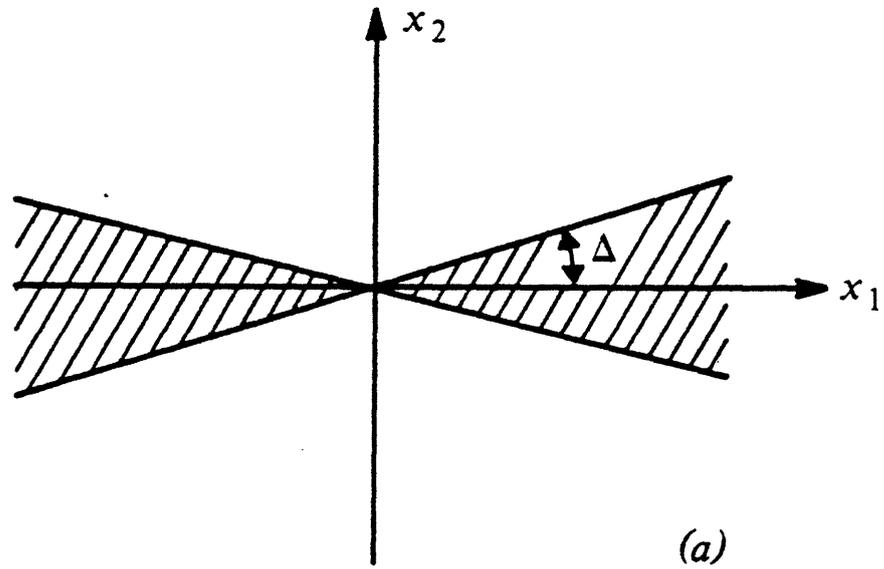
Figure 5 (a) Region where $b_{\xi,\Delta}(x)$ is nonzero.

(b) Region where $B_{\xi,\Delta}(x)$ is nonzero.
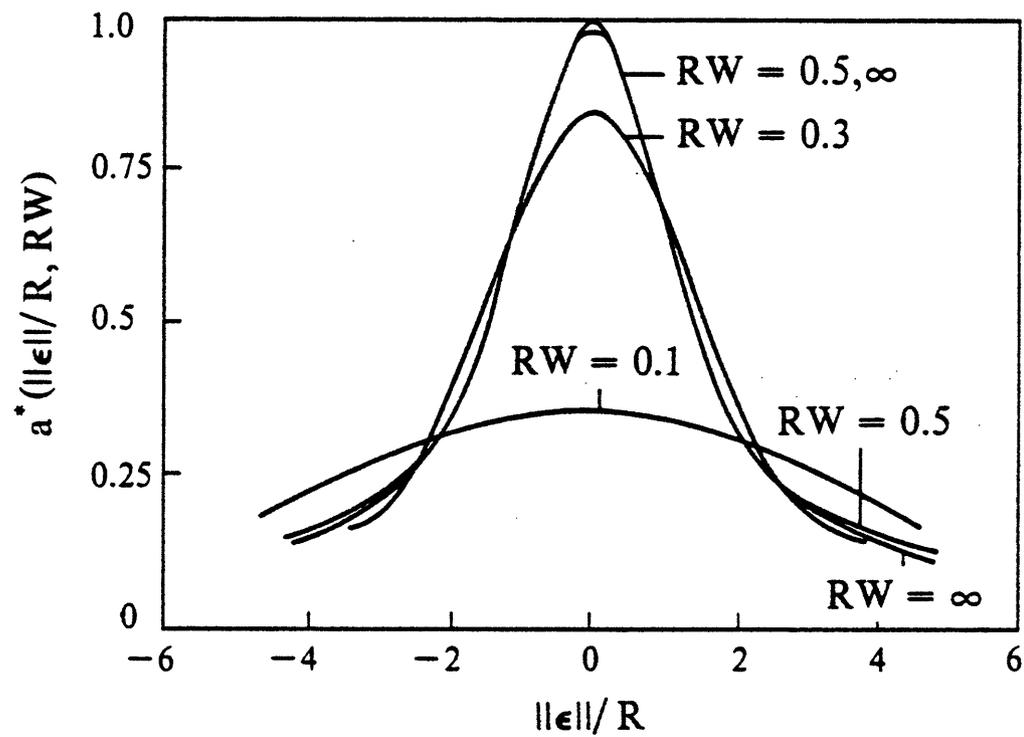
Figure 6. Central section of the normalized ambiguity function.
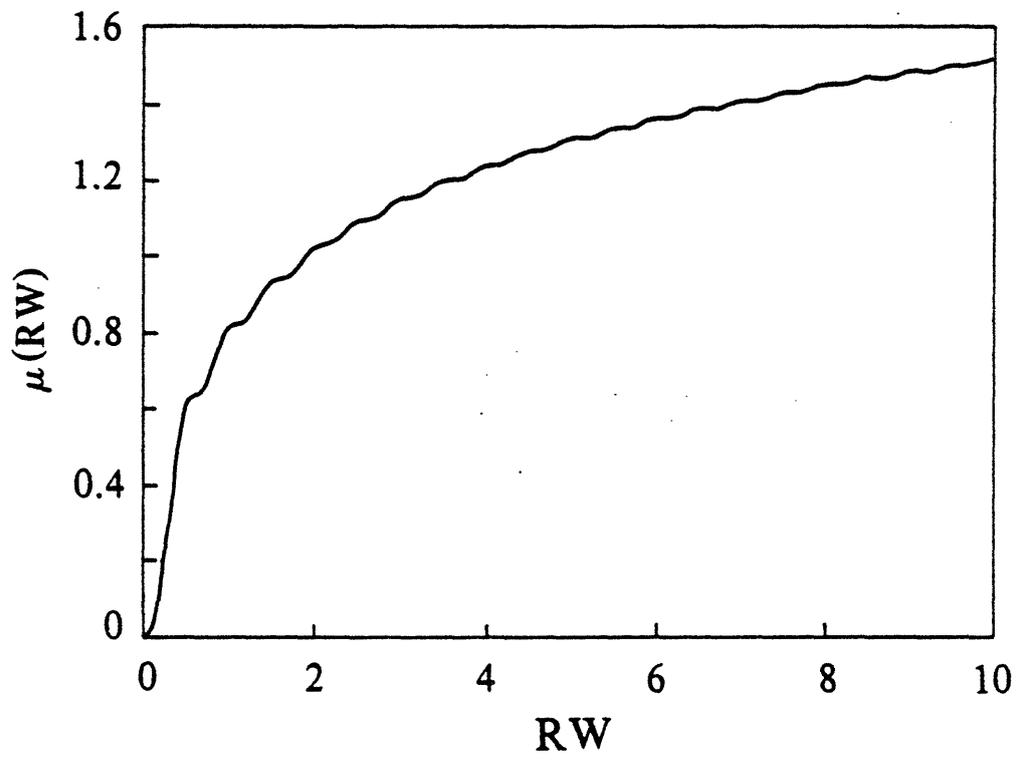
Figure 7. μ(RW) versus radius-bandwidth product.
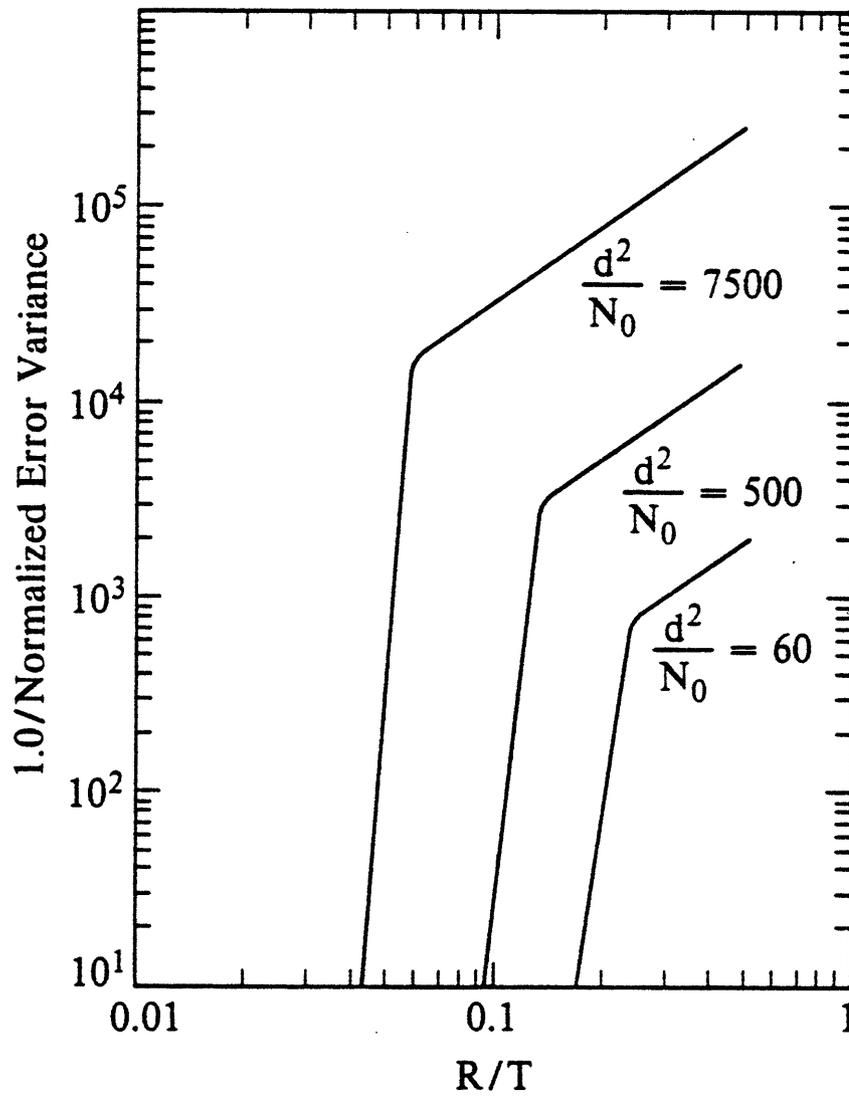
Figure 8. Localization performance versus normalized object size.
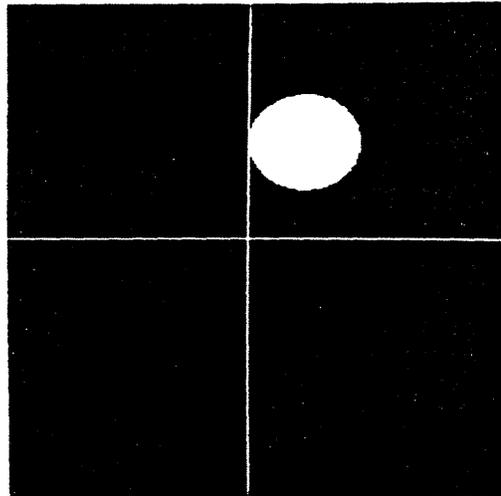
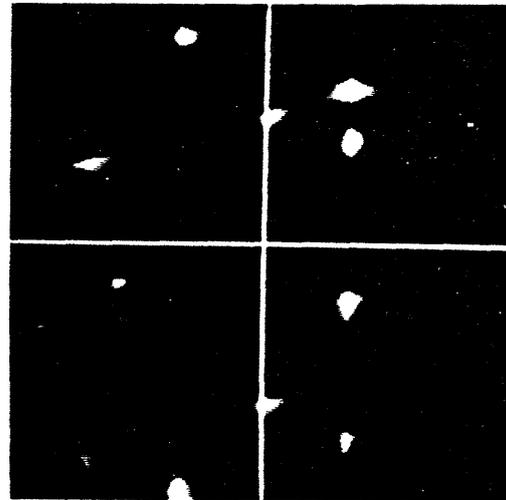Figure 9. Image representation of the single-object cross-sectional
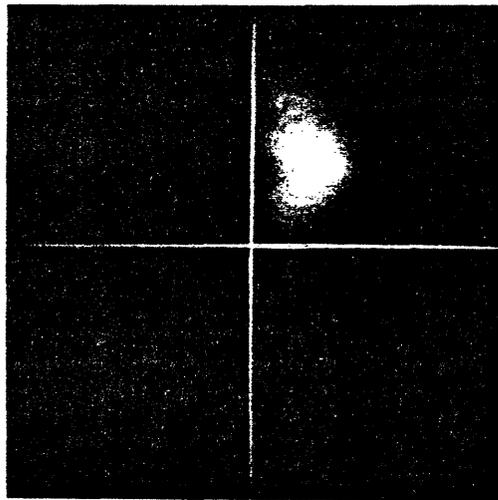
density function.
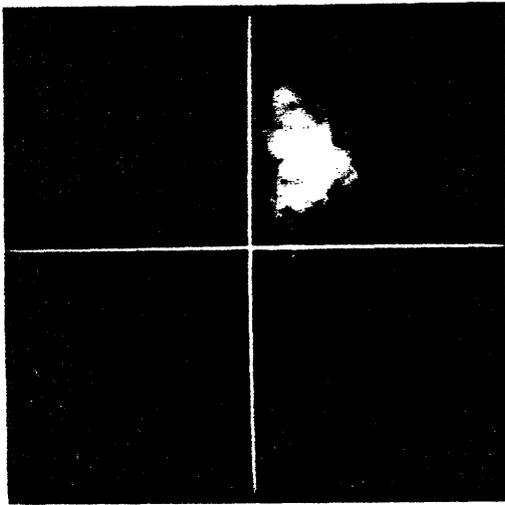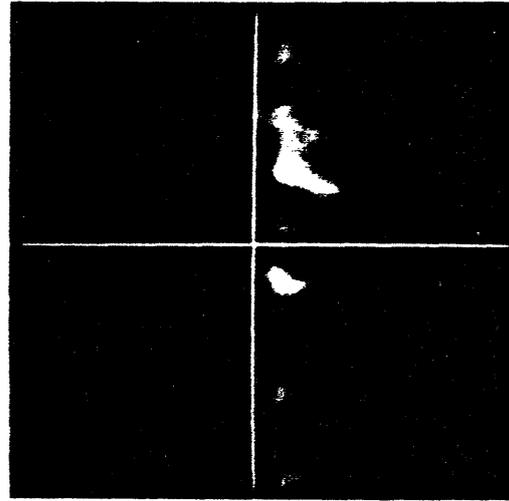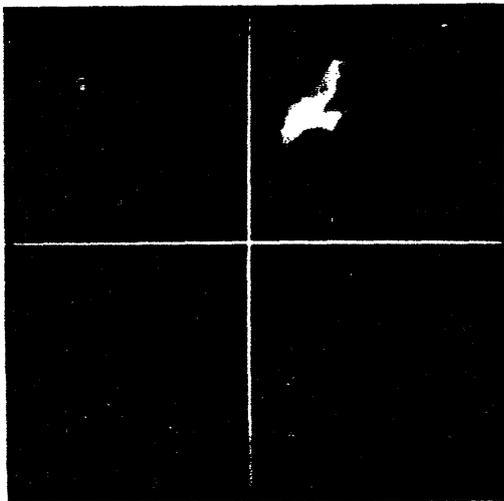
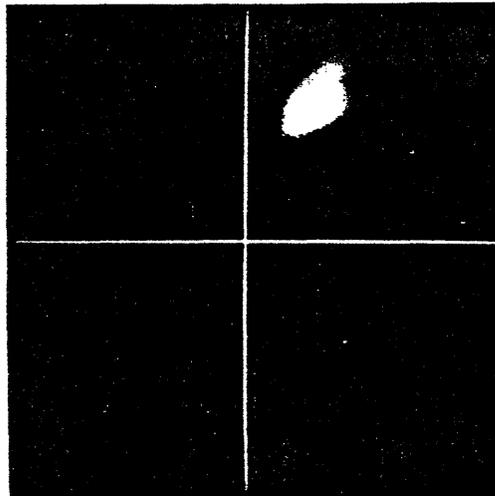Figure 10 (a) log likelihood function, SNR = 0 dB, scale = [0.6,1.0].

(b) reconstructed image, SNR = 0 dB, scale = [0.6,1.0].

(c) log likelihood function, SNR = -3 dB, scale = [0.75,1.0].

(d) reconstructed image, SNR = -3 dB, scale = [0.75,1.0].

(a)

(b)

Figure 11 (a) result of convolving the image in Figure 10b

with $f_c(x)$; scale = [0.6,1.0].

(b) result of convolving the image in Figure 10d

with $f_c(x)$; scale = [0.75,1.0].